Charge-state-dependent energy loss of slow ions. II. Statistical atom model

Richard A. Wilhelm* and Wolfhard Möller

Helmholtz-Zentrum Dresden-Rossendorf, Institute of Ion Beam Physics and Materials Research, 01328 Dresden, Germany

(Received 4 November 2015; published 16 May 2016)

A model for charge-dependent energy loss of slow ions is developed based on the Thomas-Fermi statistical model of atoms. Using a modified electrostatic potential which takes the ionic charge into account, nuclear and electronic energy transfers are calculated, the latter by an extension of the Firsov model. To evaluate the importance of multiple collisions even in nanometer-thick target materials we use the charge-state-dependent potentials in a Monte Carlo simulation in the binary collision approximation and compare the results to experiment. The Monte Carlo results reproduce the incident charge-state dependence of measured data well [see R. A. Wilhelm *et al.*, Phys. Rev. A **93**, 052708 (2016)], even though the experimentally observed charge exchange dependence is not included in the model.

DOI: 10.1103/PhysRevA.93.052709

I. INTRODUCTION

As the second part in a series of two papers we discuss here a model for charge-dependent energy loss calculation in the case of slow ions. We focus here on the dependence of energy loss on the incident ion charge state and do not take charge exchange dependence into account. Commonly energy loss is regarded as being solely dependent on the ion's effective charge alone, which results from its equilibrium charge in a solid [1]. The effective charge is only determined by the ion velocity and approaches 0 for low velocities $v \ll v_0$ (v_0 denotes the velocity of the first Bohr orbital); i.e., slow ions are regarded as neutral particles. This assumption is justified if the slow ion is initially only singly charged or transverses a long distance in a solid and thus is in charge equilibrium for a large fraction of its trajectory. However, at the surface of a solid the ion may be far from charge equilibrium, in particular, when it is initially highly charged. Experimental results on the transmission of highly charged ions through carbon foils [2–4] showed that the energy loss is strongly enhanced compared to standard SRIM values [5]. For higher ion velocities (typically MeV/amu specific kinetic energies) charge-state-dependent energy loss calculations were performed by Sigmund, Schiwietz, and others [6–10]. However, their results cannot easily be extrapolated to low velocities, which shows the need for a new approach. At low velocities only the energy loss of medium charged ions was calculated in dependence on the number of inner shell holes [11] and no universal scaling was deduced from this. Thus, we have developed a model which relies on the statistical description of atoms and ions introduced by Thomas and Fermi [12,13], which is kept rather simple and easy to handle, in contrast to expensive density functional theory calculations, which up to now cannot be used for highly charged ions [14,15].

II. CHARGE-STATE-DEPENDENT POTENTIAL

In the binary-collision picture of the transport of charged particles through matter, kinetic energy loss is determined by the interaction potential of the moving particle with its collision partners. For nonrelativistic heavy ions the problem can be described in a simple classical manner. In their statistical description of an atom with a positive nucleus and a surrounding electron cloud, Thomas and Fermi [12,13] found, for the electrostatic potential φ_{at} of a single neutral atom,

$$\varphi_{\mathrm{at}}(\vec{r}) = \varphi_{\mathrm{at}}(r) = k\frac{Ze}{r}\phi\left(\frac{r}{a_s(Z)}\right), \tag{1}$$

where Ze is the nuclear charge and $r = |\vec{r}|$ is the distance from the nucleus at $\vec{r} = 0$. The factor k refers to the Coulomb constant, which is, in SI units, $k = \frac{1}{4\pi\varepsilon_0}$. The screening function $\phi(x)$ depends on a reduced radius defined by the screening distance $a_s(Z)$, which is given by

$$a_s(Z) = \frac{3^{2/3}h^2}{2^{13/3}\pi^{4/3}m_e e^2 Z^{1/3}} = 0.8853\frac{a_0}{Z^{1/3}}, \tag{2}$$

with Planck's constant h, the electron mass m_e, the elementary charge e, and Bohr's atomic radius a_0. $\phi(x)$ solves the Thomas-Fermi-equation and has to fulfill two boundary conditions, which ensure that no screening is present at $r = 0$ and the atom is neutral at $r \to \infty$, i.e., is sufficiently screened. The latter boundary is of particular importance in Sec. IV. Several analytical approximations and numerical evaluations are available in the literature [12,13,16–19]. In their so-called similarity approach, Lindhard, Nielsen, and Scharff [20] extrapolated the Thomas-Fermi potential of a single atom [Eq. (1)] to the universal interaction potential of two atoms with the internuclear distance

$$\vec{R} = \vec{R}_p - \vec{R}_t, \tag{3}$$

where $\vec{R}_p$ and $\vec{R}_t$ denote the position of the projectile and the target atom, respectively, and nuclear charges Z_1 and Z_2 according to

$$V_{\mathrm{at}}(\vec{R}) = V_{\mathrm{at}}(R) = k\frac{Z_1 Z_2 e^2}{R}\phi_u\left(\frac{R}{a_L(Z_1,Z_2)}\right), \tag{4}$$

where the screening distance now depends on both atomic numbers according to

$$a_L(Z_1,Z_2) = 0.8853\frac{a_0}{\sqrt{Z_1^{2/3}+Z_2^{2/3}}}. \tag{5}$$

*r.wilhelm@hzdr.de

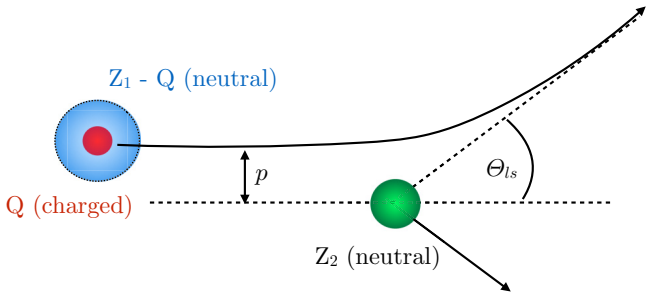

FIG. 1. Classical scattering of a charged ion with a neutral target atom. The ion, which is only partially screened, is split into a neutral atom with nuclear charge $Z_1 - Q$ and point charge Q.

From an alternative treatment of the diatomic interaction, Firsov [21] also identified Eq. (4) as a good universal approximation to the interatomic potential, with a screening length of

$$a_F(Z_1,Z_2) = 0.8853\frac{a_0}{\left(Z_1^{3/2}+Z_2^{3/2}\right)^{1/3}}. \quad (6)$$

In the following we use the so-called "universal" analytical approximation of the screening function ϕ_u by a series of exponentials according to Ziegler, Biersack, and Littmark [5,22] with the screening distance

$$a_u(Z_1,Z_2) = 0.8853\frac{a_0}{Z_1^{0.23}+Z_2^{0.23}}. \quad (7)$$

The concrete choice of the screening function (universal, Moliere [23], Kr-C [24], and others) is not important, as the long-range Coulomb interaction of the ion's charge Q dominates the scattering independently of the local character of the ion's electron cloud. So far the potentials in Eqs. (1) and (4) are only valid for scattering of neutral atoms. In the case of slow ions with velocities v well below the target's Fermi velocity v_F, an ion neutralizes along its trajectory through a solid; i.e., equilibrium is reached. Thus, the potentials derived here are well applicable. However, in the case of very thin target materials, neutralization may not be completed during transmission even for singly charged ions. Especially for slow, highly charged ions, charge states far from equilibrium are present at the surface of a solid [25] or during transmission of thin targets [2–4,26,27], which suggests a modification of the interatomic potential taking into account the charge state of the moving ion.

The basic idea to introduce the ion charge state into Eqs. (1) and (4) dates back to Brandt and Kitagawa [28] and was used in studies by Grande and Schiwietz [29] as well as Sigmund [6] and others [30,31]. The partially dressed ion in charge state Q is split virtually into a point charge Q without screening and a "virtual atom" with nuclear charge $Z - Q$ and, correspondingly, $N = Z - Q$ screening electrons. The scattering process is schematically depicted in Fig. 1. The electrostatic potential for the ion now reads

$$\varphi_{\text{ion}}(r) = k\frac{(Z-Q)e}{r}\phi\left(\frac{r}{a_s(Z-Q)}\right) + k\frac{Qe}{r}. \quad (8)$$

Since the (universal) interaction potential $V(R)$ can be written as a superposition of two different interaction potentials, $V_1(R)$ and $V_2(R)$, it changes now according to

$$\begin{aligned} V_{\text{ion}}(R) &= V_1(R) + V_2(R), \\ V_1(R) &= k\frac{(Z_1-Q)Z_2e^2}{R}\phi_u\left(\frac{R}{a_1(Z_1-Q,Z_2)}\right), \\ V_2(R) &= k\frac{QZ_2e^2}{R}\phi_u\left(\frac{R}{a_2(Z_2)}\right), \end{aligned} \quad (9)$$

with

$$\begin{aligned} a_1(Z_1-Q,Z_2) &= \frac{0.8853a_0}{(Z_1-Q)^{0.23}+Z_2^{0.23}}, \\ a_2(Z_2) &= \frac{0.8853a_0}{Z_2^{1/3}}. \end{aligned}$$

Equations (9) describe the superposition of two scattering processes, i.e., the scattering of a "virtual atom" with the screened nuclear charge $(Z - Q)$ on a neutral target with nuclear charge Z_2 $[V_1(R)]$ and the scattering of an (unscreened) point charge Q on the same target $[V_2(R)]$.

A major difference from the study by Biersack [32] is that the interaction potential $V_{\text{ion}}(R)$ is screened, as long as the target atom remains neutral and, therefore, vanishes rapidly enough for large values of R. As shown below this is a prerequisite in order to limit calculated energy transfers from elastic scattering to reasonable values.

Equations (8) and (9) now allow straightforward charge-state-dependent energy loss calculations according to standard definitions of the stopping force. This is discussed in the next two sections.

III. NUCLEAR ENERGY TRANSFER

The nuclear energy transfer is determined by two-body kinematics. From classical mechanics, the scattering angle

$$\theta_{\text{cms}}(p,E_{\text{cms}}) = \pi - 2\int_{R_{\min}}^{\infty} dR\frac{p}{R^2\sqrt{1-\frac{V(R)}{E_{\text{cms}}}-\frac{p^2}{R^2}}} \quad (10)$$

in the center-of-mass system (CMS) is given by the interaction potential $V(R)$, the impact parameter p, and the CMS kinetic energy $E_{\text{cms}} = \frac{m_2}{m_1+m_2}E_{ls}$. The particle masses are m_1 and m_2, respectively. E_{ls} is the kinetic energy in the laboratory system. The distance of closest approach $R_{\min}$ results from solving the equation

$$0 = \sqrt{1-\frac{V(R_{\min})}{E_{\text{cms}}}-\frac{p^2}{R_{\min}^2}}. \quad (11)$$

The energy transferred by a single elastic (nuclear) scattering event is given by

$$T_{\text{nucl,ls}}(p,E_{\text{cms}}) = \frac{4m_1}{(m_1+m_2)}E_{\text{cms}}\sin^2\frac{\theta_{\text{cms}}(p,E_{\text{cms}})}{2} \quad (12)$$

and the nuclear stopping cross section results:

$$S_n(E_{\text{cms}}) = 2\pi\int_0^{\infty} pT_{\text{nucl,ls}}(p,E_{\text{cms}})dp. \quad (13)$$

Using the modified charge-dependent interaction potential from Eqs. (9) in Eq. (10) allows us to obtain a charge-state-dependent nuclear stopping cross section. The nuclear

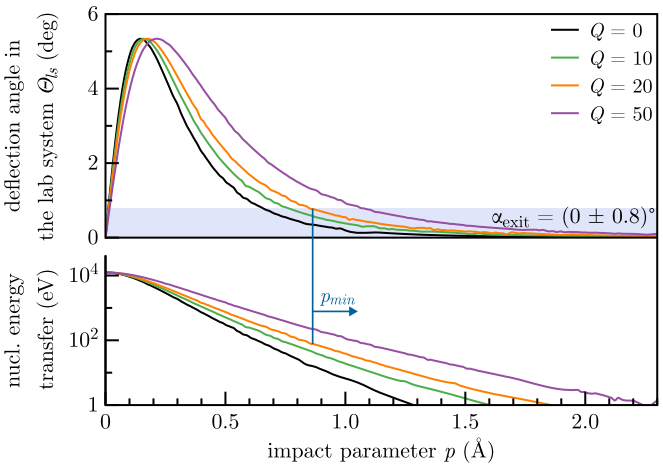

FIG. 2. Deflection angle and nuclear energy transfer as a function of the impact parameter for Xe ions scattered by carbon atoms in different charge states and an initial kinetic energy of $\varepsilon_{\text{kin}} = 310\,\text{eV/amu}$ as calculated from Eqs. (10) and (12), respectively.

transferred energies $T_{\text{nucl,ls}}$ and the scattering angle θ_{ls} are shown in Fig. 2 in the laboratory system as a function of the impact parameter p for different ion charge states Q of xenon scattering on carbon. The corresponding nuclear stopping cross section is shown in Fig. 3 as a function of the ion kinetic energy. The calculated values for $Q = 0$ are almost identical to the values taken from SRIM2013 [5]. Note that SRIM does not take ion charge states for elastic scattering into account. The stopping cross section increases for the highest charge state by a factor of 2 to 3, and the position of the maximum of the stopping cross section changes from around 200 keV for neutral xenon to about 70 keV for fully ionized xenon. The nuclear stopping force is shown in Fig. 4 as a function of the ion charge state at a fixed kinetic energy of 40 keV = 310 eV/amu (see vertical line in Fig. 3), for a carbon density of 5.54×10^{22} at/cm^3 [33]. The stopping force scales nearly

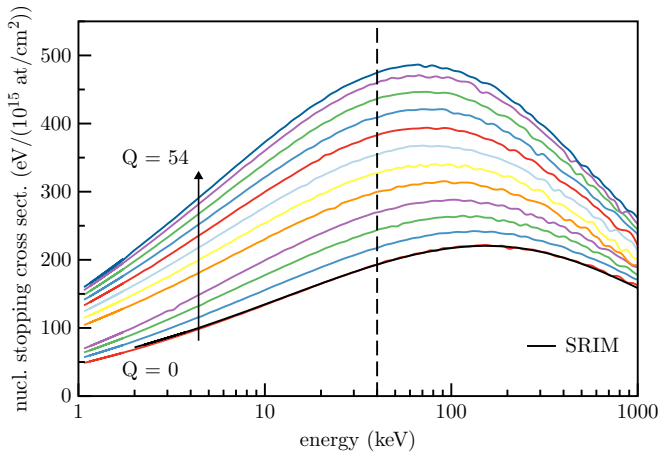

FIG. 3. Nuclear stopping cross section for xenon on carbon and different xenon charge states from Eq. (13). For comparison the nuclear stopping cross section from SRIM2013 is plotted as the black line and coincides perfectly with the calculation for $Q = 0$.

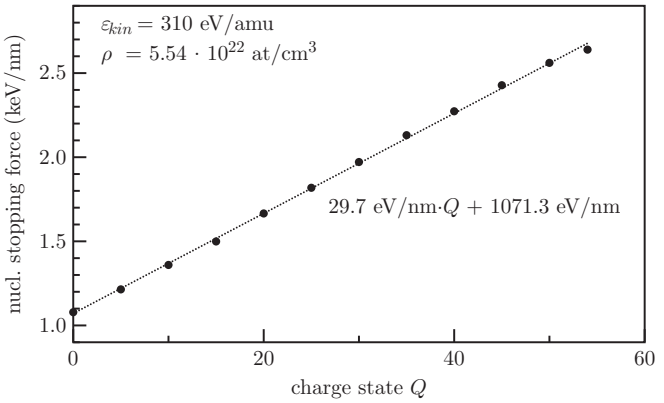

FIG. 4. Nuclear stopping force as a function of the ion charge for 310 eV/amu xenon on a carbon membrane with a density of $\varrho = 5.54 \times 10^{22}$ at/cm^3. Data points are extracted from the calculations shown in Fig. 3 (vertical line) and fitted linearly.

linearly with the charge state and increases roughly by a factor of 2.5 from $Q = 0$ to $Q = 54$ at velocities $v \ll v_0 Z_1^{2/3}$.

IV. ELECTRONIC ENERGY TRANSFER

Two approaches are available for a simplified treatment of the electronic or inelastic energy loss in the case of slow ions. Lindhard, Scharff and Schiøtt [34,35] described inelastic losses nonlocally, i.e., independently of the impact parameter. We decided to follow the model of Firsov [36]. Energy is transferred between ion and target due to electron momentum transfer across a planar surface S dividing the space into two regions, in which the electron distributions belong to either the target atom or the projectile. An electron current density between projectile and target atoms $\vec{j}(\vec{r})$ can be defined as

$$\vec{j}(\vec{r}) = \frac{n(\vec{r})\vec{v}_e(\vec{r})}{4}, \tag{14}$$

with the electron density $n(\vec{r})$ and the electron velocity $\vec{v}_e(\vec{r})$. Note that $\vec{j}$ is only defined if $\vec{r}$ is a point on the surface S. The average momentum of N exchanged electrons is given by $N\vec{p}_e = N \times m_e\vec{v}_{\text{rel}}$, where $\vec{v}_{\text{rel}}$ is the relative velocity of the projectile and target. In the case of a target atom at rest, $\vec{v}_{\text{rel}} = \vec{v}_{\text{ion}}$. Thus, the retarding force acting on the ion and leading to its energy loss is given by

$$\vec{F} = \frac{d\vec{p}_{\text{ion}}}{dt} = -m_e\vec{v}_{\text{rel}}\frac{dN}{dt} = -m_e\vec{v}_{\text{rel}}\int_S \vec{j}(\vec{r})d\vec{S}, \tag{15}$$

with $d\vec{p}_{\text{ion}} = -dN \times \vec{p}_e$. In order to evaluate Eq. (15), the electron density $n(\vec{r})$, the electron velocity $\vec{v}_e(\vec{r})$, and the surface S have to be known. The electron density and velocity could be calculated from the time-dependent density functional theory [15,37–39], but this is computationally very expensive in the case of highly charged ions. We want to focus on a simpler approach and recall again the model by Thomas and Fermi [12,13], which not only describes the Coulomb screening of atoms, but also gives a simple expression for the electron density and velocity distribution as a function of the

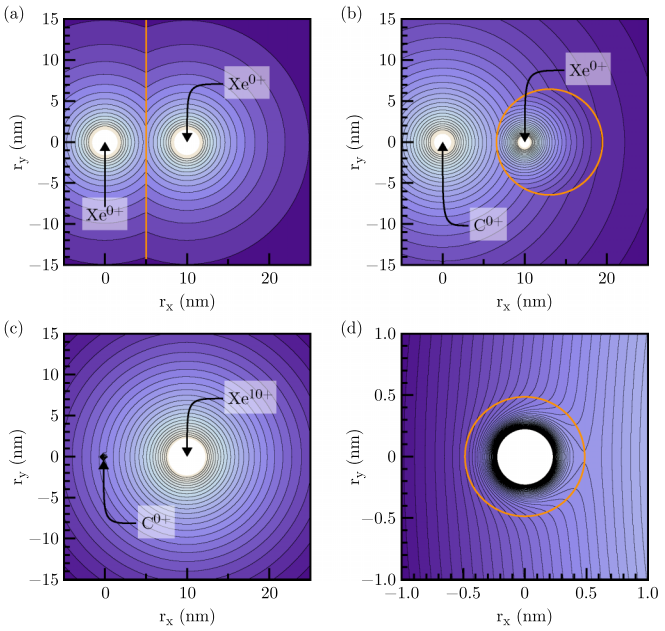

FIG. 5. Electrostatic potential $\varphi_{\text{total}}(\vec{r})$ (blue tone) with contour lines. Scattering partners are at locations $(r_x, r_y) = (0,0)$ and (10 nm,0). (a) Two equal mass particles produce a planar surface S (orange line). (b) A heavy neutral and light neutral particle produce a spherical surface S. (c) For a charged particle the potential $\varphi_{\text{ion}}(\vec{r})$ is dominated by the unscreened point charge. (d) A zoom-in around the neutral carbon atom in (c) is shown, with a spherical surface S.

atom's electrostatic potential $\varphi_{\text{at}}(\vec{r})$ [see Eq. (1)] as

$$n(r) = \frac{2^{3/2}[m_e e\varphi_{\text{at}}(r)]^{3/2}}{3\pi^2\hbar^3}, \tag{16}$$

$$|\vec{v}_e(r)| = \frac{3^{3/2}\pi\hbar n(r)^{1/3}}{4m_e}. \tag{17}$$

Assuming a linear superposition of both electron clouds to a total electron density [40–44]

$$n_{\text{total}}(r) = n_p(|\vec{r} - \vec{R}_p|) + n_t(|\vec{r} - \vec{R}_t|), \tag{18}$$

where n_p and n_t denote the electron densities of the projectile and the target atom, respectively, we can find the total electron density by using the potential for a charged ion $\varphi_{\text{ion}}(|\vec{r} - \vec{R}_p|)$ according to Eq. (8) and for a neutral atom $\varphi_{\text{at}}(|\vec{r} - \vec{R}_t|)$ according to Eq. (1) in Eq. (18) in combination with Eq. (16). Alternatively, the total potential $\varphi_{\text{total}}(\vec{r})$ can be derived by a linear superposition of φ_{ion} and φ_{at} instead of the corresponding electron densities. In this way correlations between the electron densities may be taken into account. Both ways reproduce the observed Q dependence reasonably well, so we decided to use the simpler approach.

Using n_{total} again in Eq. (16), we find the electrostatic potential $\varphi_{\text{total}}(\vec{r})$, which is plotted in Fig. 5 for three projectile-target combinations. In Fig. 5(a) two equal mass and neutral particles are located 10 nm apart from each other. (The dimensions are chosen for good representation, but the discussion is also valid for much smaller distances.) Contour lines of constant electrostatic potential are shown, which all have a kink at $r_x = 5$ nm. In Fig. 5(a), these kinks define the surface S as a planar surface in the middle between the scattering partners. Firsov already mentioned that his solution for the energy loss is only strictly valid for the case of equal mass and neutral scattering partners. Now, to extend Firsov's model, Fig. 5(b) shows a heavy neutral xenon atom and a light neutral carbon atom in the same geometry as in Fig. 5(a). The kinks of the contour lines now define a closed, spherical surface S. The surface is closed around the xenon atom, because its screening distance is much smaller ($\propto 1/Z^{1/3}$) compared to that of carbon. In the case of a charged xenon ion [Fig. 5(c)] the electrostatic potential is almost entirely dominated by the last term in Eq. (8), which is unscreened and vanishes only slowly as $1/r$. However, Fig. 5(d) shows the potential around the neutral carbon atom in more detail. Here again kinks in the contour lines are visible and define a closed spherical surface S around the carbon atom. With this way of determining the surface S and thus finding volumes in space where electrons belong to the target atom and the ion, respectively, we now can calculate the retarding force acting on the ion for every mass and charge state of the scattering partners according to Eq. (15). Note that, for simplicity, the scalar product $\vec{j}d\vec{S}$ is replaced by the product jdS assuming that the current density always points in the direction of the surface normal. This may not be true for the rear side of the surface, which may lead to an overestimation of the absolute value of the force $\vec{F}$. The electronically transferred energy in the laboratory system $T_{\text{elec,ls}}$ is given by integrating the force $\vec{F}$ along the ion trajectory $\vec{R}(t) = \vec{R}_p(t) - \vec{R}_t$. For simplicity, the trajectory is assumed to be a straight line, which is not a good assumption for very low energies. The energy transfer is then

$$\begin{aligned} T_{\text{elec,ls}}(p) &= 2\int_p^\infty |\vec{F}|dR \\ &= 2\frac{3^{1/6}m_e^2e^2}{4\pi^{5/3}\hbar^3}|\vec{v}_{\text{rel}}|\int_p^\infty\int_S \varphi_{\text{total}}^2(\vec{r})dSdR. \end{aligned} \tag{19}$$

In the case of a straight trajectory, p approximates the distance of closest approach $R_{\min}$. The factor 2 results from the fact that stopping occurs upon approach (way in) and retreat (way out) of the ion. This energy transfer depends linearly on the ion velocity, which is consistent with the literature [34,36,45], and the leading term is also proportional to Q^2. Other terms proportional to Q^m with $m < 2$ also exist, because the potential enters as φ_{total}^2. In fact, the commonly assumed quadratic dependency of the stopping on the ion charge is preserved, which is not directly obvious from Eqs. (16) and (18).

The electrostatic potential of the ion in Eq. (8) decreases slowly as $1/R$ and hence the transferred energy decreases slowly with increasing impact parameter p. This leads to very large values of $T_{\text{elec,ls}}$ even for impact parameters larger than 10 lattice constants (3 nm) and, correspondingly, to large values of the stopping force according to Eq. (13). To circumvent this problem the term $k\frac{Qe}{r}$ in Eq. (8) will be replaced by the expansion for large distances $R \gg r$ (dipole approximation [29,46]) according to

$$k\frac{Qe}{|\vec{r} - \vec{R}|} = k\frac{Qe}{R} + k\vec{r}\frac{Qe\vec{R}}{R^3} + o\left(\frac{1}{R^3}\right). \tag{20}$$

Now the integrals in Eq. (19) can be written as

$$\int_p^\infty \int_S \varphi^2_{\text{total}}(\vec{r}) dS dR = \int_p^{\varrho^{-1/3}} dR \int_S dS \varphi^2_{\text{total}}(\vec{r}) + \int_{\varrho^{-1/3}}^\infty dR \int_S dS \varphi^{*2}_{\text{total}}(\vec{r}), \tag{21}$$

with

$$\varphi^*_{\text{total}}(\vec{r}) = \frac{(3\pi^2\hbar^3 n^*_{\text{total}}(r))^{2/3}}{2m_e e}, \tag{22}$$

$$n^*_{\text{total}}(r) = n^*_p(|\vec{r} - \vec{R}_p|) + n_t(|\vec{r} - \vec{R}_t|), \tag{23}$$

and

$$\varphi^*_{\text{ion}}(|\vec{r} - \vec{R}_p|) = -k\frac{(Z_1 - Q)e}{|\vec{r} - \vec{R}_p|}\phi_u\left(\frac{|\vec{r} - \vec{R}_p|}{a_u(Z_1 - Q)}\right) - k\vec{r}\frac{Qe\vec{R}}{R^3} \tag{24}$$

as the ion's electrostatic potential at larger distances within $n^*_p(|\vec{r} - \vec{R}_p|)$ according to Eq. (16). The integral $\int dR$ is now split into two parts where the integrand is changed for $R > \varrho^{-1/3}$. The potential $\varphi^*_{\text{total}}(\vec{r})$ is the electrostatic potential in the dipole approximation, where the monopole term $\frac{Qe}{|\vec{r}-\vec{R}|}$ is replaced by the dipole term $\vec{r}\frac{Qe\vec{R}}{R^3}$, which now decreases with $1/R^2$. The distance for which this approximation is justified is here identified with the mean interatomic distance in the material, which is calculated from the material atomic density ϱ as $\varrho^{-1/3}$. In the physical picture for target-projectile distances $R > \varrho^{-1/3}$ at least one additional target atom will be located between the scattering partners and thus its electrons will screen the monopole term [47]. Only higher order terms from the expansion in Eq. (20) will then contribute, and here only the dipole term is considered. Similar approximations were done for faster ions by Grande and Schiwietz [29] and Reinhold and Burgdörfer [46]. The electronically transferred energy as a function of the impact parameter $T_{\text{elec,ls}}(p)$ in the dipole approximation is shown in Fig. 6 for different xenon charge states Q on carbon ($\varepsilon_{\text{kin}} = 310$ eV/amu). As a comparison, $T(p)$ from Firsov's equation is also shown, but as mentioned earlier for this system of unequal masses Firsov's equation may not be applicable. The values for $T_{\text{elec,ls}}(p)$ were calculated for a discrete number of impact parameters (as shown exemplarily for $Q = 30$) and then fitted by a function $a(1 + bp)^{-5}$ similar to the expression of Firsov. The fit parameters a and b have to be calculated for every charge state, projectile mass, and target mass. At around the cutoff parameter for the dipole approximation, $p_c = \varrho^{-1/3}$, the fit overestimates values for p slightly smaller, and underestimates values for p slightly larger, than p_c. However, for low charge states the transferred energies are already low (<100 eV) and thus the deviation can be neglected.

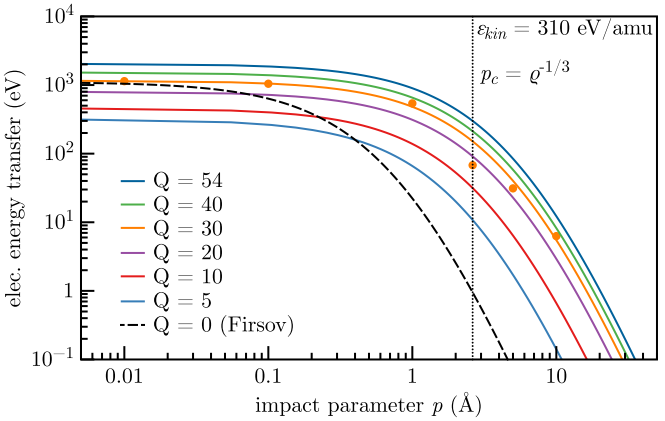

FIG. 6. Electronically transferred energy as a function of the impact parameter p for different xenon charge states on carbon. Energies are calculated for discrete impact parameters (as an example circles are shown for $Q = 30$) in the dipole approximation, Eq. (20), and fitted according to $T_{\text{elec,ls}}(p) = a(1 + bp)^{-5}$. As a comparison the result of Firsov is shown as the dashed line ($Q = 0$) [36].

V. THE ROLE OF MULTIPLE COLLISIONS

In very thin target materials and correspondingly at very low areal densities (in the range of 10^{15} at/cm^2) one could assume that only single scattering events of an ion in the target material determine the energy loss and angular distribution. To evaluate the importance of multiple collisions in a thin target material together with our charge-state-dependent model we implemented the above modified screened interaction potential [Eq. (9)] and the local electronic energy transfer [Eq. (19)], in a binary collision approximation (BCA) simulation code. According to the TRIM [22] model for an amorphous target substrate, a constant mean free path length of $\lambda_c = \varrho^{-1/3}$ between subsequent collisions is assumed. To compare the results with typical measurement conditions (see the next section), the trajectories of 10^5 xenon ions on a carbon thin film were simulated at incident kinetic energies of 40 keV (310 eV/amu), and 47 keV (364 eV/amu) and different (frozen) charge states, $Q = 10$, 20, 25, 30, and 40. Figure 7 shows the resulting energy distributions after transmission. Since the start position of each ion above the surface is chosen

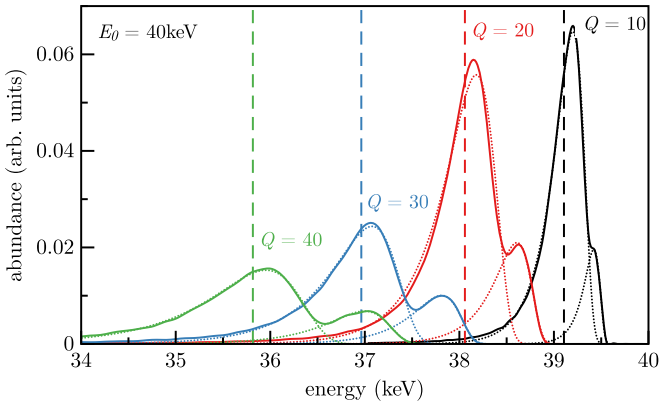

FIG. 7. Simulated energy distributions after transmission of 40-keV Xe ions at different charge states through a 1-nm-thick carbon membrane with a density of $\varrho = 5.54 \times 10^{22}$ at/cm^3 in the BCA under straightforward direction. The double-peak structure for each distribution results from three or four scattering events in the simulation. Dotted lines are Moyal fits to each peak. Dashed vertical lines are the means of each Moyal distribution.

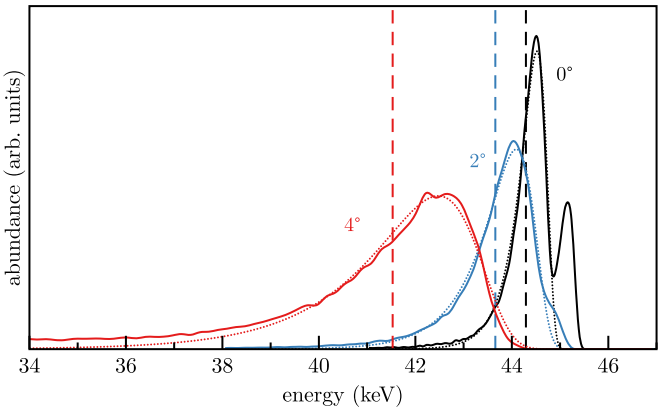

FIG. 8. Simulated energy distributions for 47-keV Xe^{25+} ions transmitted through a 1-nm-thick carbon membrane with a density of $\varrho = 5.54 \times 10^{22}$ at/cm^3 in the BCA under mean detection angles of 0° (black), 2° (blue), and 4° (red). Results are fitted with a Moyal distribution (dotted lines) and the mean value of each distribution is shown as a vertical dashed line.

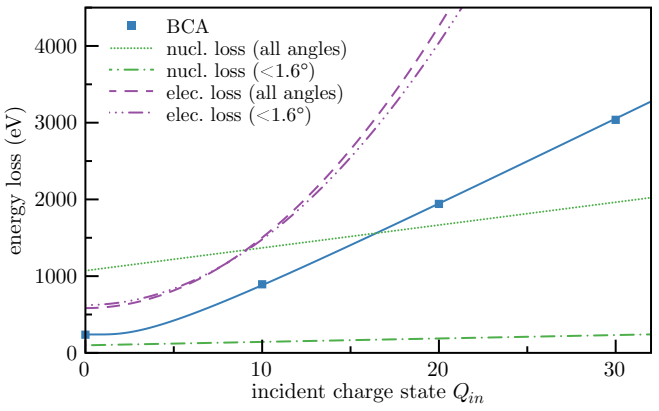

FIG. 9. Calculated energy loss values as a function of the xenon charge state, at a fixed kinetic energy of 310 eV/amu. Nuclear losses are given according to Eq. (8) (dotted line) and with selected impact parameters (dashed-dotted line) (see text). Electronic losses are given with (dashed–multidotted line) and without (dashed line) impact parameter selection. Results of our BCA simulation are shown as blue circles and are fitted with the function $\alpha Q^2 + \beta Q^{1.5} + \gamma$.

randomly, three or four scattering events are obtained, resulting in the double-peak structure shown in Fig. 7. Each peak is independently fitted by a Moyal distribution and the mean value is shown by a vertical dashed line. One clearly sees the increase in energy loss with charge state, whereas the separation by the number of scattering events becomes larger for higher Q. The BCA results here select only ions which exit the membrane within a cone of $< 1.6°$ opening angle in order to compare to measurement conditions in transmission experiments [4].

In order to make comparisons with angle-resolved measurements the resulting energy distributions were also evaluated for mean angles after transmission of $2° \pm 0.8°$ and $4° \pm 0.8°$. The respective exit energy distributions are shown in Fig. 8 for an incident kinetic energy of 47 keV (364 eV/amu) and a frozen charge state of $Q = 25$. For larger exit angles the probability of measuring ions decreases, but the energy loss significantly increases (for a fixed frozen charge state).

From the BCA results we see that the role of multiple collisions is significant already at such small target thicknesses. Under straightforward direction, for example, a single scattering approximation would result in the selection of impact parameters according to Fig. 2 ($p_{\min}$ to ∞) for nuclear and electronic losses. However, in the BCA larger impact parameters ($\hat{p} > p_{\min}$) are realized on average, because they have a higher probability, and a combination of a few large impact parameter (small-angle) scatterings would still lead to detection in certain angular acceptance regions. Thus, the convolution of only three or four scattering events during transmission can change the outcome of calculated energy losses significantly compared to the single scattering approximation.

VI. COMPARISON TO MEASURED DATA

The results obtained above are finally put into the context of a typical measurement [48] for transmission of highly charged ions through thin films. Calculated values from the statistical atom model are shown in Fig. 9. Nuclear losses according to Eq. (13) are plotted as the dotted curve. However, the integral in Eq. (13) extends over all impact parameters. In a typical measurement a detector has only a limited acceptance angle. To account for this we consider here an angular acceptance range of $< 1.6°$. Thus, in order to compare calculated losses in a single scattering approximation with measured data the integral in Eq. (13) is limited to values of p larger than $p_{\min}$ according to Fig. 2. Calculated nuclear losses accompanied by a deflection into the acceptance range of a detector are plotted in Fig. 9 as the dashed–dotted line. These losses are much smaller than the ones averaged over all impact parameters $p = 0$ to ∞, and thus we conclude that nuclear losses are enhanced by the charge state of the ion, but for transmission under a 0° exit angle only ions with small nuclear energy transfer can be measured. Calculated electronic losses are also shown, together with values taking the same impact parameter selection into account. Here differences related to an impact parameter selectivity in a measurement are small.

By selecting the impact parameters for scattering in the acceptance angle of the detector we assume a single scattering to take place. As discussed above multiple collisions can also be present here and a few small-angle scattering events are more probable than one large(r)-angle scattering. Hence, results from a BCA calculation are also shown in Fig. 9. The simulations can be fitted well with a quadratic dependence on the incident charge state and thus reproduce the dependence of data presented in part I [48].

Figure 10 shows simulated energy losses (BCA) for an incident charge state of $Q_{\text{in}} = 25$ and a kinetic energy of 364 eV/amu for xenon on carbon. The energy loss increases from 0° to 4°. Again, the overall trend of the BCA simulation using the presented model for charge-state-dependent energy loss is in agreement with measured data [4]. By assuming a single scattering event and selecting impact parameters for the angular range according to Fig. 2 the trend cannot be reproduced.

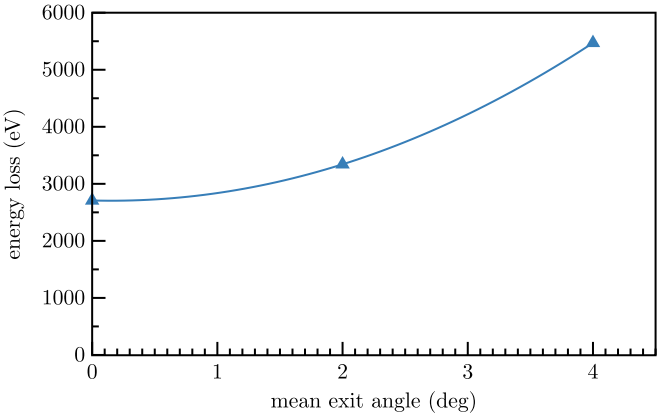

FIG. 10. Calculated energy loss as a function of the mean exit angle of Xe^{25+} ions at 364 eV/amu specific kinetic energy in the BCA (see Fig. 8). Calculated data are fitted with a quadratic function.

Note that the model above and simulations assume a frozen charge state of the incident ion and thus neglect any charge exchange processes. Consequently, they are unable to reproduce the experimentally observed strong dependence of the energy loss on the exit charge after transmission through an ultrathin carbon film as presented in part I [48]. Quantitatively, the simulation results in Fig. 9 overestimate the experimentally observed mean energy losses by a factor of about 2.5. A possible correction for charge exchange in the model is discussed in the next section, which would lead to a reduction in the predicted amount of stopping. At this point we cannot unambiguously say whether the reduction in the average charge due to charge exchange or multiple collisions (larger average impact parameters) plays the major role in experiment. One should also note that the ion will be in a highly excited electronic state during transmission, which affects the form of the electrostatic potential and thus the energy loss as well.

The main conclusion from this section is that measured energy losses for slow, highly charged ions under 0° observation will mainly result from electronic losses. The picture changes for larger angles, where nuclear losses may dominate. For applications such as ion implantation and nanostructure formation, only the total amount of deposited energy in a certain depth is important. In this case, i.e., when the angular distribution of ions does not matter, nuclear losses contribute significantly for heavy xenon on carbon at energies below 100 keV up to $Q \approx 10$ (see Fig. 9). For even higher charge states electronic losses dominate the kinetic energy transfer.

VII. POSSIBLE COUPLING TO CHARGE EXCHANGE

As discussed above, the large values of the calculated electronic energy transfer from the presented statistical atom model may be due to the neglect of charge exchange. Treating the ion in a frozen charge state does not take observed charge exchange into consideration. A very simple approach to determining charge exchange cross sections in the case of close collisions is the method of molecular orbital diagrams, originally introduced by Fano and Lichten [49] and adapted for highly charged ions by Stolterfoht and Arnau [30,50–52]. In this so-called screened hydrogen model, shifts of the ion and target orbitals can be determined. At very close interparticle distances the orbitals may diverge and the ion states are shifted up into the valence band of the target material. Under these conditions multiple charge transfer could occur, as suggested by Arnau *et al.* [30]. No hollow atom will be formed due to this charge exchange process, because inner shell levels will directly be populated. This will also limit processes by which the highly charged ion will emit secondary electrons. Now, energy loss calculations can be redone using the critical distance for a large level shift into the valence band R_c from molecular orbital diagrams to set the ion charge to 0 if $R < R_c$. In this case the ion charge is on average lower than the incident charge along the trajectory, which reduces the calculated electronic losses.

VIII. SUMMARY AND CONCLUSION

By introducing the simple approximation of an ion in a charge state Q being replaced by a neutral atom of atomic charge $(Z - Q)$ and point charge Q as written in Eqs. (8) and (9), we can show that nuclear as well as electronic energy transfer is strongly enhanced for slow, highly charged ions. We conclude that electronic energy loss is the dominant dissipation channel for highly charged ions ($Q > 20$). Employing a simulation in the BCA allows us to estimate the importance of multiple scattering and the simulation reproduces trends in measured data reasonably well. Charge exchange is so far not included in the model, whereas it heavily affects measurements.

Further improvement of the model may involve a better choice of the screening function $\phi_u(x)$ for the case of heavy projectiles on light targets, the consideration of the electron current flow direction $\vec{j}/j$ in Eq. (15), and the use of detailed molecular orbital diagrams directly from Hartree-Fock calculations.

ACKNOWLEDGMENTS

Financial support from the Deutsche Forschungsgemeinschaft (DFG; Project No. HE 6174/1-1) is acknowledged.

[1] N. Bohr and J. Lindhard, Mat. Meddelelser K. Danske Vidensk. Selsk. **28**, 1 (1954).

[2] T. Schenkel, M. A. Briere, A. V. Barnes, A. V. Hamza, K. Bethge, H. Schmidt-Böcking, and D. H. Schneider, Phys. Rev. Lett. **79**, 2030 (1997).

[3] T. Schenkel, A. Hamza, A. Barnes, and D. Schneider, Prog. Surf. Sci. **61**, 23 (1999).

[4] R. A. Wilhelm, E. Gruber, R. Ritter, R. Heller, S. Facsko, and F. Aumayr, Phys. Rev. Lett. **112**, 153201 (2014).

[5] J. F. Ziegler, J. P. Biersack, and M. D. Ziegler, *SRIM: The Stopping and Range of Ions in Matter* (SRIM Co., Chester, MD, 2008).
[6] P. Sigmund, Phys. Rev. A **56**, 3781 (1997).
[7] G. Schiwietz and P. L. Grande, Nucl. Instrum. Methods Phys. Res. Sec. B Beam Interact. Mater. Atoms **153**, 1 (1999).
[8] T. Kaneko, Phys. Rev. A **49**, 2681 (1994).
[9] G. Maynard, K. Katsonis, C. Deutsch, G. Zwicknagel, M. Chabot, and D. Gardès, Nucl. Instrum. Methods Phys. Res. Sec. A Accel. Spectrom. Detect. Assoc. Equip. **464**, 86 (2001).
[10] G. Maynard, G. Zwicknagel, C. Deutsch, and K. Katsonic, Phys. Rev. A **63**, 052903 (2001).
[11] J. I. Juaristi, A. Arnau, P. M. Echenique, C. Auth, and H. Winter, Phys. Rev. Lett. **82**, 1048 (1999).
[12] L. H. Thomas, Math. Proc. Cambridge Philos. Soc. **23**, 542 (1927).
[13] E. Fermi, Z. Phys. **48**, 73 (1928).
[14] O. Lehtinen, J. Kotakoski, A. V. Krasheninnikov, A. Tolvanen, K. Nordlund, and J. Keinonen, Phys. Rev. B **81**, 153401 (2010).
[15] Z. Wang, S.-S. Li, and L.-W. Wang, Phys. Rev. Lett. **114**, 063004 (2015).
[16] R. P. Feynman, N. Metropolis, and E. Teller, Phys. Rev. **75**, 1561 (1949).
[17] G. Molière, Z. Naturforsch. **2A**, 133 (1947).
[18] W. Lenz, Z. Phys. **77**, 713 (1932).
[19] H. Jensen, Z. Phys. **77**, 722 (1932).
[20] J. Lindhard, V. Nielsen, and M. Scharff, Mat. Meddelelser Udgivet Af Det K. Danske Vidensk. Selsk. **36**, 1 (1968).
[21] O. B. Firsov, Sov. Phys. JETP-USSR **6**, 534 (1958).
[22] J. F. Ziegler, J. P. Biersack, and U. Littmark, *The Stopping and Range of Ions in Solids (Vol. 1. Stopping and Range of Ions in Solids)*, edited by J. Ziegler (Pergamon Press, New York, 1985).
[23] R. D. Reed and J. S. Nodvik, Phys. Rev. **135**, B199 (1964).
[24] W. D. Wilson, L. G. Haggmark, and J. P. Biersack, Phys. Rev. B **15**, 2458 (1977); L. Vinet and A. Zhedanov, J. Phys. A: Math. Theor. **44**, 085201 (2011).
[25] S. Winecki, C. L. Cocke, D. Fry, and M. P. Stöckli, Phys. Rev. A **53**, 4228 (1996).
[26] R. A. Wilhelm, E. Gruber, R. Ritter, R. Heller, A. Beyer, A. Turchanin, N. Klingner, R. Hübner, M. Stöger-Pollach, H. Vieker, G. Hlawacek, A. Gölzhäuser, S. Facsko, and F. Aumayr, 2D Mater. **2**, 035009 (2015).
[27] R. A. Wilhelm, A. S. El-Said, F. Krok, R. Heller, E. Gruber, F. Aumayr, and S. Facsko, Prog. Surf. Sci. **90**, 377 (2015).
[28] W. Brandt and M. Kitagawa, Phys. Rev. B **25**, 5631 (1982).
[29] P. L. Grande and G. Schiwietz, Phys. Rev. A **58**, 3796 (1998).
[30] A. Arnau, R. Köhrbrück, M. Grether, A. Spieler, and N. Stolterfoht, Phys. Rev. A **51**, R3399 (1995).
[31] N. R. Arista, Nucl. Instrum. Methods Phys. Res. Sec. B Beam Interact. Mater. Atoms **195**, 91 (2002).
[32] J. P. Biersack, Nucl. Instrum Methods Phys. Res. Sec. B Beam Interact. Mater. Atoms **80-81**, 12 (1993).
[33] D. G. Matei, N.-E. Weber, S. Kurasch, S. Wundrack, M. Woszczyna, M. Grothe, T. Weimann, F. Ahlers, R. Stosch, U. Kaiser, and A. Turchanin, Adv. Mater. **25**, 4146 (2013).
[34] J. Lindhard and M. Scharff, Phys. Rev. **124**, 128 (1961).
[35] J. Lindhard, M. Scharff, and H. E. Schiøtt, Mat. Meddelelser Udgivet Af Det K. Danske Vidensk. Selsk. **33**, 1 (1963).
[36] O. B. Firsov, Sov. Phys. JETP **36**, 1076 (1959).
[37] W. Kohn and L. J. Sham, Phys. Rev. **140**, A1133 (1965).
[38] W. Kohn, Rev. Mod. Phys. **71**, 1253 (1999).
[39] A. Ojanperä, A. V. Krasheninnikov, and M. Puska, Phys. Rev. B **89**, 035120 (2014).
[40] R. G. Gordon, J. Chem. Phys. **56**, 3122 (1972).
[41] P. Loftager, F. Besenbacher, O. S. Jensen, and V. S. Sørensen, Phys. Rev. A **20**, 1443 (1979).
[42] J. Biersack and J. Ziegler, Nucl. Instrum. Methods Phys. Res. **194**, 93 (1982).
[43] S. M. Foiles, M. I. Baskes, and M. S. Daw, Phys. Rev. B **33**, 7983 (1986).
[44] M. S. Daw and M. I. Baskes, in *Chemistry and Physics of Fracture*, edited by R. M. Latanision and R. H. Jones (Kluwer Academic, Hingham, MA, 1987), pp. 196–218.
[45] D. Primetzhofer, S. Rund, D. Roth, D. Goebl, and P. Bauer, Phys. Rev. Lett. **107**, 163201 (2011).
[46] C. O. Reinhold and J. Burgdörfer, J. Phys. B At. Mol. Opt. Phys. **26**, 3101 (1993).
[47] Note that in the case of slow ions $v_{\text{ion}} \ll v_0$ and thus electron rearrangement is adiabatic.
[48] R. A. Wilhelm, E. Gruber, V. Smejkal, S. Facsko, and F. Aumayr, Phys. Rev. A **93**, 052708 (2016).
[49] U. Fano and W. Lichten, Phys. Rev. Lett. **14**, 627 (1965).
[50] N. Stolterfoht, in *Progress in Atomic Spectrosccopy: Part D*, edited by H. J. Beyer and H. Kleinpoppen (Springer US, Boston, MA, 1987), p. 415.
[51] N. Stolterfoht, A. Arnau, M. Grether, R. Köhrbrück, A. Spieler, R. Page, A. Saal, J. Thomaschewski, and J. Bleck-Neuhaus, Phys. Rev. A **52**, 445 (1995).
[52] A. Arnau, F. Aumayr, P. M. Echenique, M. Grether, W. Heiland, J. Limburg, R. Morgenstern, P. Roncin, S. Schippers, R. Schuch, N. Stolterfoht, P. Varga, T. J. M. Zouros, and H. P. Winter, Surf. Sci. Rep. **27**, 113 (1997).